OPEN ACCESS



Observational Analysis and Numerical Modeling of the Solar Wind Fluctuation Spectra during Intervals of Plasma Instability

S. A. Markovskii and Bernard J. Vasquez

Space Science Center, University of New Hampshire, Durham, NH 03824, USA; sergei.markovskii@unh.edu, bernie.vasquez@unh.edu Received 2022 July 31; revised 2022 October 24; accepted 2022 October 31; published 2022 December 13

Abstract

We perform a statistical analysis of observed magnetic spectra in the solar wind at 1 au with localized power elevations above the level of the ambient turbulent fluctuations. We show that the elevations are seen only when the intensity of the ambient fluctuations is sufficiently low. Assuming that the spectral elevations are caused by thermal-ion instabilities, this suggests that on average the effect of the solar wind background is strong enough to suppress the instability or obscure it or both. We then carry out nonlinear numerical simulations with particle ions and an electron fluid to model a thermal-ion instability coexisting with an ambient turbulence. The parameters of the simulation are taken from a known solar wind interval where an instability was assumed to exist based on the linear theory and a bi-Maxwellian fit of the observed distribution with core and secondary-beam protons. The numerical model closely matches the position of the observed spectral elevation in the wavenumber space. This confirms that the thermal-ion instability is responsible for the elevation. At the same time, the magnitude of the elevation turns out to be smaller than in the real solar wind. When higher intensity of the turbulence is used in the simulation, which is typical of solar wind in general, the power elevation is no longer seen. This is in agreement with the reduced observability of the elevations at higher intensities. However, the simulations show that the turbulence does not simply obscure the instability but also lowers its saturation level.

Unified Astronomy Thesaurus concepts: Space plasmas (1544); Interplanetary turbulence (830); Solar wind (1534)

1. Introduction

The solar wind is characterized by a variety of fluctuations. Some of the main processes responsible for the fluctuations are a turbulent energy cascade and plasma instabilities. The turbulent fluctuations produce a power-law spectrum over a wide range of scales (Coleman 1968). Instabilities are observed as localized power elevations above the turbulence spectrum at the ion kinetic scales (Behannon 1976; Tsurutani et al. 1994). Whether these fluctuations coexist independently or have some effect on each other is not well understood.

At 1 au, the instabilities responsible for the power elevations are likely driven by thermal-ion distribution functions (Jian et al. 2014), in particular, their temperature anisotropy and relative drifts of the ion species. Interstellar pickup ions also cannot be ruled out as a source of the enhanced wave power. However, Fisher et al. (2016) found only three such events per year. The occurrence rate of the power elevations is much higher (Jian et al. 2009). Therefore, one has to assume that most of them are caused by something other than the pickup ions.

The instabilities in the solar wind develop in a turbulent ambient medium. The turbulence produces spatially nonuniform and time-dependent fluctuations. Therefore, the instability may not behave in the same way as it would in a homogeneous and stationary medium. The characteristic time of the turbulence can be estimated as the nonlinear eddy turnover time for the kinetic scales, at which the instability is growing (Markovskii et al. 2006). If it is comparable to or smaller than the instability growth time, then the variation of the

Original content from this work may be used under the terms of the Creative Commons Attribution 4.0 licence. Any further distribution of this work must maintain attribution to the author(s) and the title of the work, journal citation and DOI.

background is significant and has to be taken into account (Mikhailenko & Stepanov 1984; Maslennikov et al. 1995; Markovskii & Hollweg 2002). The inhomogeneity is also an essential factor (Ozak et al. 2015; Hellinger et al. 2017; Ofman et al. 2017; Markovskii et al. 2019a). In particular, it can make the unstable waves more oblique, thereby changing the character of the wave–particle interaction and the resulting particle heating (Markovskii et al. 2019a).

The power elevations associated with the pickup ions have been observed only when the turbulence is relatively weak (Cannon et al. 2014; Aggarwal et al. 2016; Fisher et al. 2016; Hollick et al. 2018). During these events the energy transfer rate of the turbulent cascade was smaller than the rate of the wave energy production by the pickup ions, while during control events it was larger. The cascade energy transfer rate and the turbulent eddy turnover time are related parameters, but the latter is a local characteristic in the wavenumber space, while the former is global. Another factor that affects the observability of the spectral elevations is the spacecraft sampling angle with respect to the mean magnetic field. They are seen preferentially at small angles in a wide range of heliocentric distances (Murphy et al. 1995; Jian et al. 2009, 2014; Boardsen et al. 2015; Bowen et al. 2020). At larger angles, the waves responsible for the elevations may be obscured or suppressed by the turbulent fluctuations.

The interpretation of the observed thermal-ion instabilities in the solar wind is usually based on a linear theory and on the assumption of a homogeneous and stationary background (Gary et al. 2015; Jian et al. 2016; Bowen et al. 2020). In the present paper, we analyze the relevant statistical properties of the observed magnetic spectra with power elevations at 1 au. We then use this information along with one sample solar wind interval to compare the spectra with numerical simulations. The

simulations include a turbulent ambient medium and describe the nonlinear evolution the instability.

2. Data Description

We used 92 ms magnetic field data obtained by Wind spacecraft (Lepping et al. 1995; Koval & Szabo 2013) between 2005 January 1 and 2005 May 31. During this period, the spacecraft was located near the L1 point. The solar wind intervals to calculate the power spectra were taken to be 100 minutes. On the one hand, this duration is sufficiently long to cover large enough scales at which the spectrum can be fitted to a power law. On the other hand, the frequency range in such an interval is not much larger than the one that we obtain from our numerical simulations. The five-month period of data is chosen to be roughly in the same phase of the solar cycle as the one sample on 2005 March 19, in which we directly compare the observed spectrum with numerical simulations.

An automated search for statistical outliers in the data was made in each magnetic field component in two passes. At first, the entire interval considered for the spectrum was examined, and individual measurements providing the data points outside of 3.5 standard deviation from the average were flagged. Then, the interval was divided in 200 s subintervals, and the process was repeated for each subinterval and a standard deviation of 3.0. Typically, 1% to 3% of the data points were excluded this way.

The spectra were computed with the help of the Blackman–Tukey algorithm (Blackman & Tukey 1958), which gives the Fourier transform of the correlation tensor of the magnetic field $\langle B_i B_j \rangle$, modified by Chen (1989, Section 5.2; see also the Appendix in Bieber et al. 1993). Instead of the original time series of the magnetic field B(t), Chen (1989) introduced a new series of vector differences between successive data points ΔB $(t) = B(t + \Delta t) - B(t)$. Here Δt is the temporal separation between the data points. Next, the Fourier transform was taken of the correlation function of the differences $\langle \Delta B_i \Delta B_j \rangle$. The power spectrum of the magnetic field P_B was then derived from the trace of the differences spectrum S_{tr} according to the formula

$$P_B(\nu) = \frac{S_{tr}}{4\sin^2(\pi\nu\Delta t)}.$$
 (1)

To interpret the properties of the fluctuation spectra, we need to know the solar wind parameters of the corresponding intervals. For this purpose, we used 92 s plasma data obtained by Wind spacecraft (Ogilvie et al. 1995). The observed quantities relevant to our study are the solar wind velocity and density derived from nonlinear fitting to the ion-current distribution function. The intervals were accepted only if they had at least 40 valid measurements, although the coverage was better in most cases. In the sample solar wind interval, for which we make a detailed comparison with numerical simulations, we also used the parameters of the proton distribution function as described below. These parameters, derived from the Wind spacecraft data, are published by Gary et al. (2015).

3. Observational Results

The subject of our analysis is magnetic spectra with elevated power above the ambient turbulence level presumably caused by a plasma instability. We select spectra that obey a power law

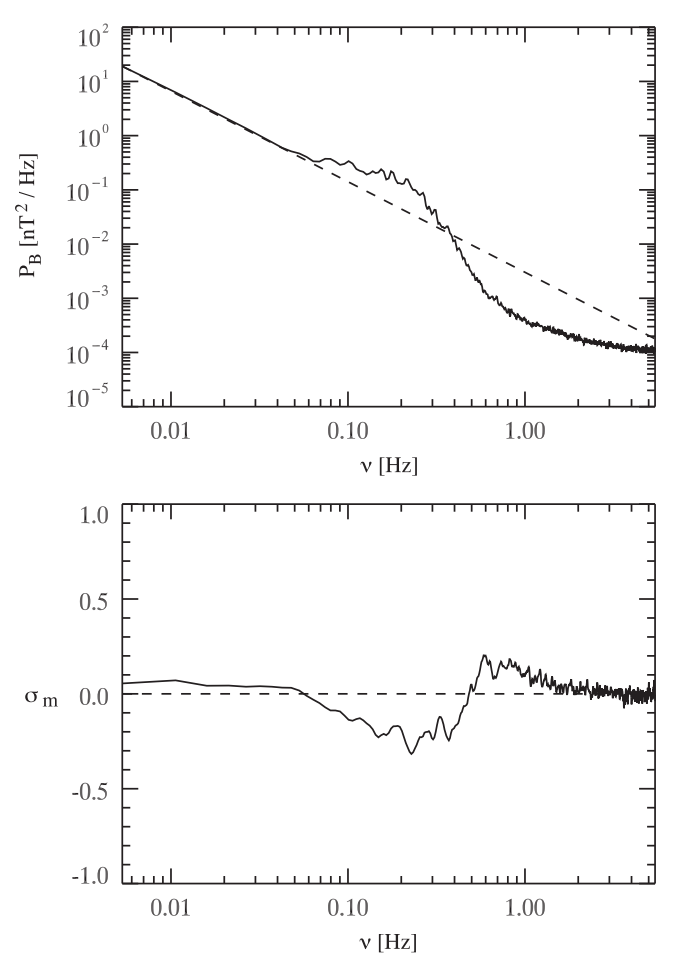


Figure 1. Sample magnetic power P_B and magnetic helicity σ_m spectra with a power elevation. The dashed line in the top panel is a least-squares power-law fit. The dashed line in the bottom panel shows a zero helicity value for reference.

at lower frequencies and have a "bump" at higher frequencies, i.e., a localized power increase with respect to an extrapolation of that power law. An example of this kind of spectrum is shown in the top panel of Figure 1. We perform an unconstrained least-squares power-law fit in the range $0.0053~{\rm Hz} < \nu < 0.032~{\rm Hz}$, where ν is the spacecraft frequency. To quantify the quality of the fit to the observed spectrum, we use the Pearson product–moment correlation coefficient R, as described by Markovskii et al. (2008). For all the spectra in our data set, $|R| \geqslant 0.97$.

We consider a spectral elevation observed if the excess power is comparable to the background level. We checked that at least at some ν within the elevation the total power was twice as high as the power associated with the power-law fit at that frequency. For comparison with the solar wind in general, we fitted with a power law the spectra in the rest of the available intervals. The spectra without the elevation usually have a break at the ion kinetic scales, which separate a shallower spectral slope at lower frequencies from a steeper slope at higher frequencies (Figure 2, top panel). When the break was present, the range 0.0053 Hz < ν < 0.032 Hz was always in the shallower portion of the spectrum.

The intervals with the elevated magnetic power typically show a sign reversal of the magnetic helicity spectrum σ_m (Figure 1, bottom panel). Here σ_m was calculated from a reduced spectrum of an off-diagonal component of a two-point

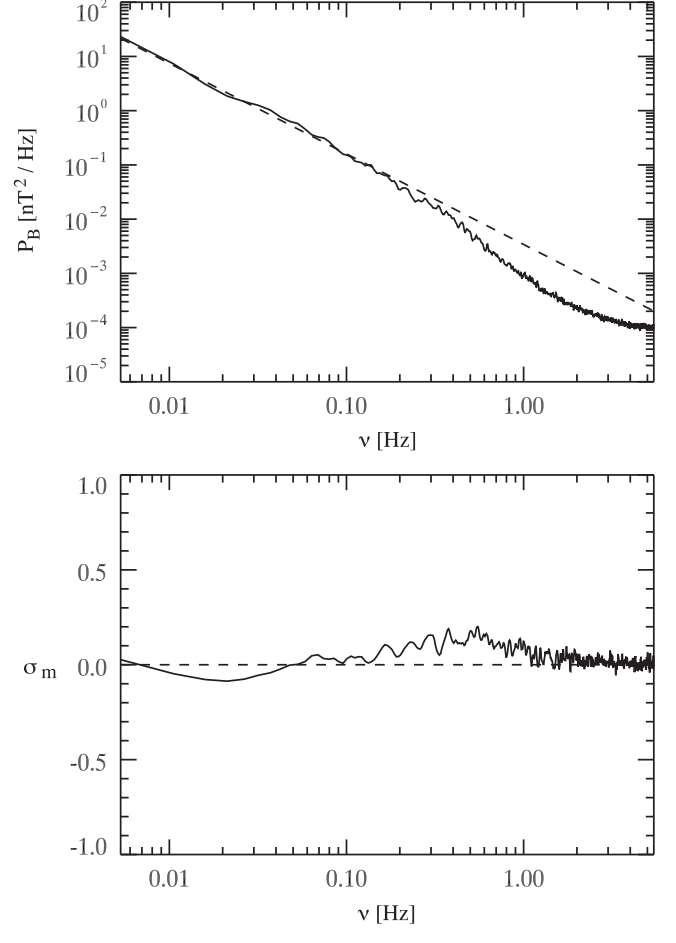


Figure 2. Same as Figure 1 but showing a sample without a power elevation.

correlation function of the magnetic field $\langle B_T B_N \rangle$ in the RTN coordinate system (Matthaeus et al. 1982)

$$\sigma_m(\nu) = 2 \operatorname{Im}[\langle B_T B_N \rangle] / P_B, \tag{2}$$

and the magnetic field measured by Wind in the geocentric solar ecliptic (GSE) coordinates was transformed to the radial-tangential-normal (RTN) coordinates with the help of the ephemeris data.

The magnetic helicity signatures of the solar wind turbulence have been studied by Markovskii et al. (2015, 2016) and Telloni et al. (2015), and more details can be found in these references. The turbulence can produce a nonzero magnetic helicity even if it is purely two-dimensional in the plane perpendicular to the mean magnetic field B_0 and no propagating linear waves exist in the system (Markovskii & Vasquez 2013, 2016). The sign reversal seen in Figure 1 may indicate a configuration including separate helicity signatures associated with the turbulence and a plasma instability. These signatures can aid the search of the spectral power elevations. However, not all instabilities produce magnetic helicity, and it was not taken into account in the present analysis.

We recorded 74 intervals with a spectral elevation, compared to a total number of 1916 in the solar wind in general, suggesting an occurrence rate of about 4%. The average spectral slopes of the power-law fits were -1.67 and -1.62 in the former and the latter groups, respectively. To quantify the intensity of the background fluctuations in each interval, we use

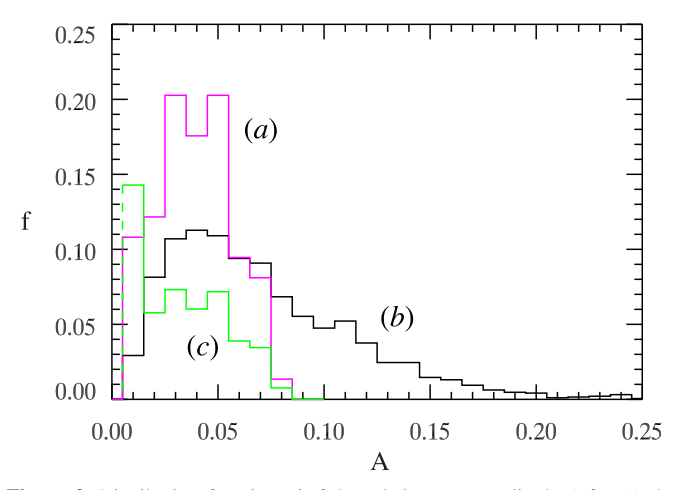


Figure 3. Distribution functions f of the relative rms amplitude A for (a) the intervals with power elevations (magenta line) and (b) the solar wind in general (black line). The distributions are normalized to the total number of intervals in each case. The green line (c) is the distribution with power elevations normalized to the distribution in the solar wind in general.

the following procedure. We pick a certain scale and estimate the rms amplitude of the fluctuations at that scale for all the spectra. The scale has to be expressed in terms of plasma parameters rather than the spacecraft frequency to characterize the relevant physical processes. Since the observed spectra will be later compared to numerical simulations, as a reference wavenumber, we chooe the wavenumber that will be used to initiate the turbulence in the simulations, namely, $k_0 = 0.083 \ d_p^{-1}$, where d_p is the inertial length calculated from the proton density averaged over the 100 minute intervals.

To convert k_0 to the spacecraft frequency ν_0 , we assume that Taylor's frozen-in hypothesis is valid and the turbulent fluctuatons at this scale are quasi-two-dimensional with the wavevectors nearly perpendicular to the mean magnetic field B_0 . Then,

$$\nu_0 = \frac{k_0 V_{\text{SW}} \sin(\theta)}{2\pi},\tag{3}$$

where the solar wind speed $V_{\rm SW}$ is directly averaged over the interval, and the angle θ between the sampling direction and \boldsymbol{B}_0 is calculated after averaging the three components of the magnetic field. The quantity ν_0 was always outside of the localized spectral elevation when it was present. When the elevation was absent, ν_0 was always lower than the break frequency of the spectrum, at which its slope becomes steeper compared to the range $0.0053~{\rm Hz} < \nu < 0.032~{\rm Hz}$. Once the spectrum is fitted to a power law P in the range $0.0053~{\rm Hz} < \nu < 0.032~{\rm Hz}$, the relative rms amplitude of the magnetic field A is evaluated according to the formula

$$A = \frac{\sqrt{P(\nu_0) \,\nu_0}}{B_0}.\tag{4}$$

Figure 3 displays the distribution functions of A for the intervals with spectral power elevations and for the solar wind in general, i.e., all the intervals with or without the elevations. As can be seen from the figure, the former distribution is cut off at high amplitudes, as opposed to the latter. The average values for these distributions are 0.039 and 0.072, and the standard deviations are 0.018 and 0.048, respectively. We have used Welch's unequal variances test (Welch 1947) to verify that a

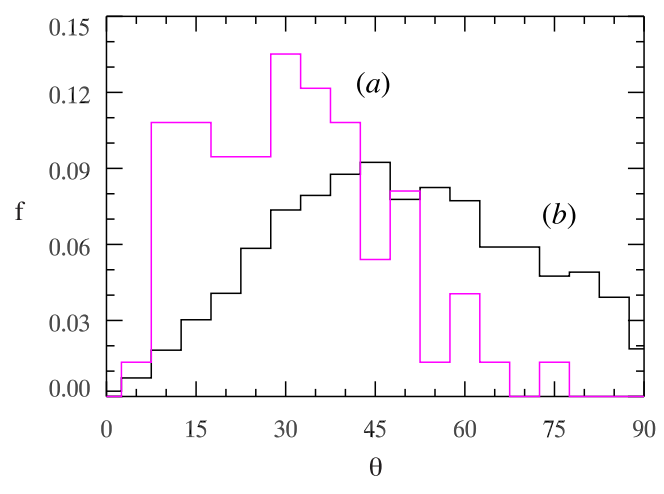


Figure 4. Distribution functions f of the angle between the mean magnetic field and the spacecraft sampling direction for (a) the intervals with power elevations (magenta line) and (b) the solar wind in general (black line). The distributions are normalized to the total number of intervals in each case.

sufficient number of statistical samples have been collected and the difference between the averages is statistically significant.

As discussed in the introduction, the observability of the instability is also affected by the spacecraft sampling direction with respect to the mean magnetic field. Figure 4 shows the distributions of the sampling angle θ of the intervals with power elevations and the solar wind in general. The distributions are again normalized to the total number of intervals in each case. The distribution with power elevations is shifted to smaller angles with respect to the general one, in agreement with the known results (Murphy et al. 1995; Jian et al. 2009, 2014; Boardsen et al. 2015; Bowen et al. 2020). However, one can show that the observability is not reduced to the sampling direction effect alone. To eliminate this effect and compare the intervals with and without instability in the same range of θ , we have separated out a subset of the intervals in the solar wind in general with the sampling angle limited to moderately oblique directions $\theta < 50^{\circ}$. The resulting modified distribution of A is practically the same as the original one in Figure 3 (black line), and our conclusion that the power elevations are observed only at low A remains valid.

4. Numerical Modeling

We will now consider a specific example of the solar wind interval with a power elevation and compare it with a numerical simulation. We choose one of the intervals discussed by Gary et al. (2015) and use the data published in their paper to model their Event #1 on 2005 March 19 (78.380 < DOY < 78.389). Based on a bi-Maxwellian fit, the instability during this event is driven by the temperature anisotropy of the core proton distribution. The streaming of a secondary proton beam and alpha particles with respect to the core protons breaks the symmetry of the instability and makes the growth rates of wave propagating in sunward and antisunward directions unequal.

To reduce the computational cost of the simulations, we neglect the alpha particles and only keep the secondary proton beam. We also assume a somewhat higher proton core temperature anisotropy $T_{\perp c}/T_{\parallel c}=2.5$ than an observed value

of 2.24. The other necessary parameters are as follows: the proton core density $n_{0c}=3.2~{\rm cm}^{-3}$; the parallel core plasma beta $\beta_{\parallel c}=0.14$; the beam-to-core number density ratio $n_{0b}/n_{0c}=0.4$; the relative beam/core drift speed $V_d=0.8V_A$, where V_A is defined with the proton core number density n_{0c} ; the parallel beam-to-core temperature ratio $T_{b\parallel}/T_{c\parallel}=2.9$; the beam temperature anisotropy $T_{b\perp}/T_{b\parallel}=0.94$; the mean magnetic field $B_0=8.1~{\rm nT}$; the sampling angle $\theta=39^\circ$; and the proton core speed along the Sun–Earth line $V_c=400~{\rm km}~{\rm s}^{-1}$.

These parameters are used to initiate three-dimensional (3D) hybrid simulations with particle-in-cell protons and a quasineutralizing electron fluid. The numerical code was developed by Terasawa et al. (1986) and Vasquez (1995, 2015). Our setup has been described in detail by Markovskii et al. (2019b, 2020) and Markovskii & Vasquez (2022a, 2022b), and more information can be found in those references. To simplify the numerical model, the electron temperature and mass are set to zero. The simulation grid is 128 cells in all three directions. The simulation box size is $L_{\parallel}=128$ in the x-direction, and $L_{\perp}=64$ in the y- and z-directions in units of the proton inertial length $V_A \Omega_p^{-1}$. The gyrofrequency Ω_p is defined with the initial mean value of the magnetic field B_0 , pointing in the x-direction. The proton core and beam distribution functions are loaded as spatially uniform drifting bi-Maxwellians. The drift speed of the proton core $V_{dc} = 0$, and beam $V_{db} = 0.8V_A$. The initial ion number densities and temperatures are uniform. The number of proton core and beam particles per cell is 2000 and 1000, respectively.

We initiate a turbulent cascade with seed fluctuations at the low-wavenumber end of the spectrum. To evaluate the relative initial rms amplitude of the magnetic field fluctuations, we use the spectrum presented by Gary et al. (2015). The magnetic power spectral density $P(0.01) = 20 \, \mathrm{nT}^2/\mathrm{Hz}$ at a spacecraft frequency of $\nu = 0.01 \, \mathrm{Hz}$. At larger frequences, P follows approximately the Kolmogorov slope. Our own calculation of the observed spectrum in this interval gives practically the same quantitative result as that of Gary et al. (2015), as will be seen below.

We then put $V_{\rm SW} = V_c$ in Equation (3) because our simulation is in the proton core frame of reference. From here and Equation (4),

$$A \equiv \left[\frac{1}{128^3} \sum_{\mathbf{x}} \frac{|\Delta \mathbf{B}(0, \mathbf{x})|^2}{B_0^2} \right]^{1/2} = 0.038, \tag{5}$$

where the magnetic field fluctuation $\Delta \mathbf{B}(t, \mathbf{x})$ at the initial moment of time t = 0 is given by the formula

$$\Delta \boldsymbol{B}(0, \boldsymbol{x}) = \frac{1}{2} \sum_{\boldsymbol{k}} [\delta \boldsymbol{B}(0, \boldsymbol{k}) \exp(i(\boldsymbol{k} \cdot \boldsymbol{x} + \phi(\boldsymbol{k}))) + \text{c.c.}].$$
(6)

Here ${\pmb x}$ is the Cartesian spatial position vector, ${\pmb k}$ is the wavevector, and $\phi({\pmb k})$ is a random phase. The seed spectrum of the turbulence is confined to the modes $({\pmb k}_x=0,{\pmb k}_y=\pm 2\pi/L_\perp,{\pmb k}_z=\pm 2\pi/L_\perp)$. The proton core and beam velocity fluctuations $\Delta {\pmb V}_{c,b}$ are defined in the same way as $\Delta {\pmb B}$ in Equation (6). The components of the vectors $\delta {\pmb B}(0,{\pmb k})$ and $\delta {\pmb V}_{c,b}(0,{\pmb k})$ obey the polarization relations of linear Alfvén waves in the cold MHD limit.

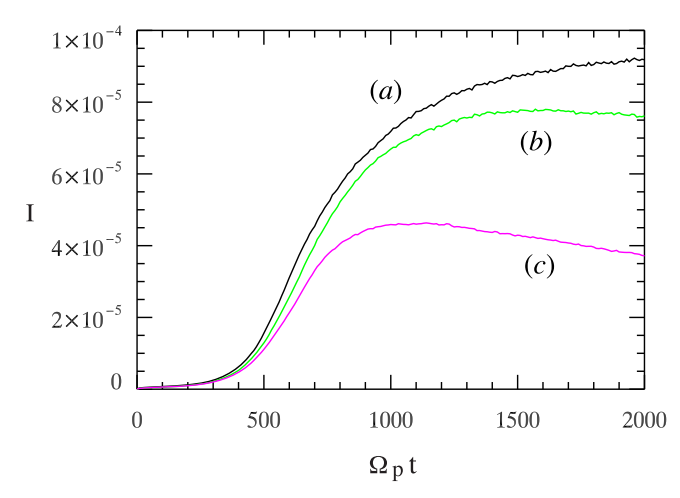


Figure 5. Time dependence of the total intensity I of the unstable magnetic fluctuations, normalized to B_0^2 , corresponding to an initial turbulence amplitude of (a) A=0 (black line), (b) A=0.038 (green line), and (c) A=0.072 (magenta line).

In our setup, a turbulence highly oblique to the mean magnetic field develops from the seed spectrum before the instability grows to a significant level. After that, the instability keeps growing and eventually saturates. The turbulence affects the instabilities driven by ion-temperature anisotropy and ion beams by reducing the growth rate or the saturation level or both (Markovskii et al. 2019b, 2020; Markovskii & Vasquez 2022a, 2022b). In the present case, the instability produces nearly parallel-propagating Alfvén waves, and the mirror modes are not excited. The turbulence and instability are well separated in the wavenumber space because of the orientation of their wavevectors with respect to the mean magnetic field. Therefore, we can calculate the total intensity I of the instability at a given time by summing only the intensities of the spatial Fourier modes $|\delta \mathbf{B}|^2$ in the subspace of the wavenumber space occupied by the unstable fluctuations.

The quantity *I* is plotted in Figure 5 as a function of time. As can be seen from the figure,

The quantity A in our sample interval is close to an average value of 0.039 for the intervals with the spectral elevation. In this case, the difference between the green and black curves in Figure 5 is not too large, so the effect of the turbulence is not very strong. To compare it to the solar wind in general, we ran a simulation with A = 0.072 equal to the average value for all the spectra regardless of the elevation. This produced a much stronger effect (magenta curve in Figure 5).

We will now compare the spectra resulting from the simulations to the observed one (Figure 6). To model the observations, we ran an artificial spacecraft probe through the simulation box. In order to get more statistical data, the probe was run along multiple lines perpendicular to the z-axis and inclined at an angle of 39° to the x-axis. This is the angle between the sampling direction and the mean magnetic field during the observed interval. The spectra calculated that way were averaged over all the trajectories. The reduced spectra were further averaged over the time intervals in the saturation phase where the intensity of the unstable waves was not changing much, namely, $1000 \le t \Omega_p \le 1700$ in cases (b) and (c) in Figure 6 and $800 \le t \Omega_p \le 1500$ in case (d). The wavenumbers in the simulations were converted back to the spacecraft frequency with the help of Equations (3) and (4) and

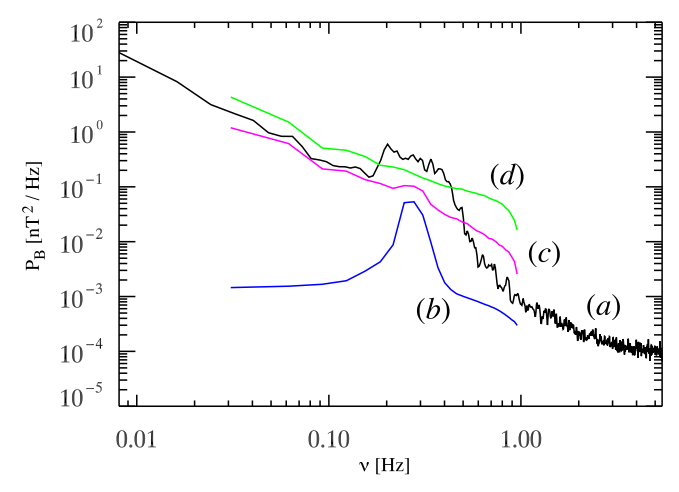


Figure 6. Reduced magnetic power spectra from (a) the observational data, (b) the simulation with A=0 (blue line), (c) A=0.038 (magenta line), and (d) A=0.072 (green line).

the parameters of the observed interval. To establish a correspondence between the discrete numerical spectrum and its continuous counterpart, we divide the power by the frequency spacing between the discrete modes, which is equal to the lowest frequency in our numerical system $\nu_0 = 0.0031\,\mathrm{Hz}$.

With the realistic parameters used in the simulations, the numerical model (the magenta line (c) in Figure 6) accurately reproduces the position of the observed spectral elevation (the black line (a) in Figure 6) on the frequency axis. For reference, we show the power peak associated with the instability without turbulence (the blue line (b) in Figure 6). The turbulence spectrum at lower frequencies outside of the elevation also matches closely. However, the magnitude of the elevation is smaller than the observed one. This suggests that the instability in the solar wind is stronger than in the numerical model. One of the possible reasons is that the actual distribution function is not described by a bi-Maxwellian with core and beam components, as was assumed in the interpretations of the observational data.

The green curve (d) in Figure 6 demonstrates the effect of a higher turbulence intensity on the instability. In this hypothetical case, where the intensity would be the same as in the average solar wind, the spectral elevation is not visible.

We also note that the spectral elevation in our simulations disappears when the sampling angle θ approaches 90° (not shown). This behavior is in qualitative agreement with the results of Hellinger et al. (2019).

5. Conclusion

We have performed a statistical analysis of observed magnetic spectra with a power elevation at 1 au. We have shown that the elevations are seen only when the intensity of the ambient solar wind fluctuations is sufficiently low. The intensity is defined at a fixed small faction of the inverse proton inertial scale so that the scale is outside of the power elevation range. There is a statistically significant difference between the average intensities for the intervals with a power elevation and the solar wind in general. Assuming that the spectral elevations are caused by thermal-ion instabilities, this suggests that on

average the effect of the background solar wind is strong enough to suppress the instability or obscure it or both.

We have then carried out nonlinear numerical simulations with particle ions and a quasi-neutralizing electron fluid to model a thermal-ion instability coexisting with an ambient turbulence. The parameters of the simulation were taken from a known solar wind interval where an instability was assumed to exist based on the linear theory and a bi-Maxwellian fit of the observed distribution function with core and secondary-beam protons. The intensity of the turbulence also matched the observed value, which was close to the average intensity among the spectra with power elevations. We have found that the turbulence reduces the saturation level of the instability but not by much. We have also run a simulation with the turbulence intensity equal to the average value in the solar wind in general. This produced a much larger reduction of the saturation level.

To compare the observed spectra with the numerical model, we used an artificial spacecraft probe in our simulations to calculate a reduced spectrum along the same sampling direction with respect to the mean magnetic as the observed one. The simulations produce a spectrum that closely matches the position of the observed spectral elevation in the wavenumber space. This confirms that the thermal-ion instability is responsible for the elevation. At the same time, the magnitude of the elevation in the numerical model turns out to be smaller. It is not clear why the instability in the actual solar wind is stronger, and further investigation of this issue is needed. It is possible that the measured ion distribution function is more complex than the assumed fit. When the higher intensity of the turbulence is used in the simulation, the power elevation is no longer seen. This is in agreement with the reduced observability of the elevations at higher intensities. However, the simulations show that the turbulence does not just obscure the instability but also lowers the intensity of the unstable fluctuations.

The Wind spacecraft data were obtained from CDAWeb (https://cdaweb.gsfc.nasa.gov). The authors are grateful to the Wind/IMF and Wind/SWE teams for making the data available. This work was supported by NASA Heliophysics Supporting Research Program under grants 80NSSC21K1674 and 80NSSC19K0832 and by the NSF SHINE Program under grant AGS2005982 to the University of New Hampshire. The simulations were performed on Marvin, a Cray CS500 supercomputer at the University of New Hampshire. Marvin is supported by the NSF Major Research Instrumentation Program under grant AGS1919310.

ORCID iDs

Bernard J. Vasquez https://orcid.org/0000-0001-8593-7289

References

```
Aggarwal, P., Taylor, D. K., Smith, C. W., et al. 2016, ApJ, 822, 94
Behannon, K. W. 1976, PhD thesis, National Aeronautics and Space
   Administration, Goddard Space Flight Center
Bieber, J. W., Chen, J., Matthaeus, W. H., Smith, C. W., & Pomerantz, M. A.
  1993, JGR, 98, 3585
Blackman, R. B., & Tukey, J. W. 1958, The measurement of power spectra
  (New York: Dover Publications)
Boardsen, S. A., Jian, L. K., Raines, J. L., et al. 2015, JGRA, 120, 10207
Bowen, T. A., Mallet, A., Huang, J., et al. 2020, ApJS, 246, 66
Cannon, B. E., Smith, C. W., Isenberg, P. A., et al. 2014, ApJ, 787, 133
Chen, J. 1989, PhD thesis, University of Delaware
Coleman, P. J. 1968, ApJ, 153, 371
Fisher, M. K., Argall, M. R., Joyce, C. J., et al. 2016, ApJ, 830, 47
Gary, S. P., Jian, L. K., Broiles, T. W., et al. 2015, JGRA, 121, 30
Hellinger, P., Landi, S., Matteini, L., Verdini, A., & Franci, L. 2017, ApJ,
Hellinger, P., Matteini, L., Landi, S., et al. 2019, ApJ, 883, 178
Hollick, S. J., Smith, C. W., Pine, Z. B., et al. 2018, ApJ, 863, 76
Jian, L. K., Moya, P. S., Viñas, A. F., & Stevens, M. 2016, in AIP Conf. Proc.
   1720, Fourteenth International Solar Wind Conference, ed. L. Wang et al.
  (Melville, NY: AIP), 040007
Jian, L. K., Russell, C. T., Luhmann, J. G., et al. 2009, ApJ, 701, L105
Jian, L. K., Wei, H. Y., Russell, C. T., et al. 2014, ApJ, 786, 123
Koval, A., & Szabo, A. 2013, in AIP Conf. Proc. 1539, Thirteenth International
   Solar Wind Conference, ed. G. Zank et al. (Melville, NY: AIP), 211
Lepping, R. P., Acuna, M. H., Burlaga, L. F., et al. 1995, SSRv, 71, 207
Markovskii, S. A., Chandran, B. D. G., & Vasquez, B. J. 2019a, ApJ, 870, 121
Markovskii, S. A., & Hollweg, J. V. 2002, JGRA, 107, 1329
Markovskii, S. A., & Vasquez, B. J. 2013, ApJ, 768, 62
Markovskii, S. A., & Vasquez, B. J. 2016, ApJ, 820, 15
Markovskii, S. A., & Vasquez, B. J. 2022a, ApJ, 924, 111
Markovskii, S. A., & Vasquez, B. J. 2022b, ApJ, 930, 120
Markovskii, S. A., Vasquez, B. J., & Chandran, B. D. G. 2019b, ApJ, 875, 125
Markovskii, S. A., Vasquez, B. J., & Chandran, B. D. G. 2020, ApJ, 889, 7
Markovskii, S. A., Vasquez, B. J., & Smith, C. W. 2008, ApJ, 675, 1576
Markovskii, S. A., Vasquez, B. J., & Smith, C. W. 2015, ApJ, 806, 78
Markovskii, S. A., Vasquez, B. J., & Smith, C. W. 2016, ApJ, 833, 212
Markovskii, S. A., Vasquez, B. J., Smith, C. W., & Hollweg, J. V. 2006, ApJ,
  639, 1177
Maslennikov, D. I., Mikhailenko, V. S., & Stepanov, K. N. 1995, PlPhR,
  21, 749
Matthaeus, W. H., Goldstein, M. L., & Smith, C. W. 1982, PhRvL, 48, 1256
Mikhailenko, V. S., & Stepanov, K. N. 1984, ZhETF, 87, 161
Murphy, N., Smith, E. J., Tsurutani, B. T., Balogh, A., & Southwood, D. J.
   1995, SSRv, 72, 447
Ofman, L., Viñas, A. F., & Roberts, D. A. 2017, JGRA, 122, 5839
Ogilvie, K. W., Chornay, D. J., Fritzenreiter, R. J., et al. 1995, SSRv, 71, 55
Ozak, N., Ofman, L., & Viñas, A.-F. 2015, ApJ, 799, 77
Telloni, D., Bruno, R., & Trenchi, L. 2015, ApJ, 805, 46
Terasawa, T., Hoshino, M., Sakai, J.-I., & Hada, T. 1986, JGR, 91, 4171
Tsurutani, B. T., Arballo, J. K., Mok, J., et al. 1994, GeoRL, 21, 633
Vasquez, B. J. 1995, JGR, 100, 1779
Vasquez, B. J. 2015, ApJ, 806, 33
Welch, B. L. 1947, Biometrika, 34, 28
```